AIP Advances

Turbulent flow of liquid lead alloy in oxygen-controlled corrosion erosion test facility

Cite as: AIP Advances **11**, 075303 (2021); https://doi.org/10.1063/5.0057380
Submitted: 20 May 2021 . Accepted: 16 June 2021 . Published Online: 02 July 2021

Renate Fetzer, Alfons Weisenburger, and Georg Mueller

Turbulent flow of liquid lead alloy in oxygen-controlled corrosion erosion test facility

Cite as: AIP Advances 11, 075303 (2021); doi: 10.1063/5.0057380
Submitted: 20 May 2021 • Accepted: 16 June 2021 •
Published Online: 2 July 2021

Renate Fetzer,[a] Alfons Weisenburger, and Georg Mueller

AFFILIATIONS

Institute for Pulsed Power and Microwave Technology (IHM), Karlsruhe Institute of Technology (KIT), Hermann-von-Helmholtz-Platz 1, 76344 Eggenstein-Leopoldshafen, Germany

[a]Author to whom correspondence should be addressed: renate.fetzer@kit.edu

ABSTRACT

The CORELLA (CORrosion Erosion test facility for Liquid Lead Alloy) facility allows corrosion erosion tests in molten lead alloys at controlled oxygen content and temperature under flowing conditions. Its exposure chamber consists of a cylindrical container, partially filled with the liquid metal. An inner rotating cylinder drives the liquid metal flow. The specimens of interest are fixed vertically inside the chamber such that the lead alloy flows around the specimens on both sides. In this numerical study, the turbulent flow of liquid lead–bismuth eutectic is solved for various specimen configurations, filling heights, and rotational speeds of the inner cylinder. Hereby, the deformation of the free liquid surface is taken into account using a rotationally symmetric approximation. Highly turbulent flow is found even for 200 rpm (revolutions per minute), the lowest rotational speed investigated. The velocity of the liquid metal along the specimens' lateral surfaces reaches values up to 1.5 m/s for a rotational speed of 1200 rpm, the limit of experimentally stable conditions. Due to the sudden flow constrictions and expansions around the specimens, a much higher effect of the flow on corrosion erosion is expected than for simple pipe flow at the same bulk velocity.

I. INTRODUCTION

Because of their excellent thermal properties, heavy liquid metals (HLMs) gain more and more importance as heat transfer and storage media in energy-related technologies, such as concentrating solar power, Generation-IV fast reactors, and accelerator-driven systems.[1,2] A major drawback of HLMs, such as molten Pb or lead–bismuth eutectic (LBE), is their aggressiveness toward structural materials. The high solubility of steel alloying elements in Pb or LBE at elevated temperature can lead to selective dissolution and HLM penetration, combined with structural and phase changes, deterioration of mechanical properties, and finally failure.[3–5] One mitigation technique of liquid metal corrosion is the *in situ* growth of a protective oxide layer on the surfaces of exposed materials and components.[6–9] Hereby, a low oxygen content in the liquid Pb or LBE and a specific material composition (at the surface) guarantee a controlled oxidation process in terms of the oxidation rate and the type of oxide grown.[10–12]

In addition to the corrosion behavior in static HLMs experimentally investigated in a vast number of studies for numerous materials, the behavior in flowing HLMs is of utmost importance for technological implementation. Depending on the velocity of the HLM, erosion may take place at the material surfaces and the combined corrosion erosion process needs to be studied. One example of a test stand designed to perform isothermal corrosion erosion tests in lead alloys with controlled oxygen content and flow velocity is the CORELLA (CORrosion Erosion test facility for Liquid Lead Alloy) facility at the Karlsruhe Institute of Technology (KIT), Germany.[13] It consists of two chambers, one for conditioning the lead alloy in terms of the oxygen content, the other for the exposure experiment under flowing conditions. Both chambers are covered with gas tight lids. Once the HLM in the conditioning chamber reaches the targeted oxygen content, it is pumped to the exposure chamber previously loaded with the specimens of interest. This second chamber consists of a cylindrical container and a rotating inner cylinder. The specimens are fixed to sample holders, which are mounted to a plate underneath the lid. Technically, the rotational speed of the inner cylinder can be set to values up to 2000 rpm (revolutions per minute). However, stable flow conditions without sloshing are obtained up to about 1200 rpm, depending on

the filling height and on the dimensions and the number of specimens inserted. A detailed description of the entire setup of the CORELLA facility is provided in Ref. 13, together with some preliminary simulations of the flow field inside the exposure chamber. This preliminary computational fluid dynamics (CFD) work considered an empty chamber without any obstacles, i.e., without specimens or sample holders inserted, and assumed laminar flow, an approximation that turned out to be not accurate at all. Therefore, the preliminary results should be understood as a very rough guide only. The grown interest in the CORELLA facility in recent years made a more accurate calculation of the flow field necessary.[14] The current study therefore presents a detailed numerical investigation of the liquid lead alloy flow inside the exposure chamber of the CORELLA facility, taking into account turbulence, a consistent treatment of the free liquid surface, and the loading of the chamber with sample holders and specimens. The objective is to get reliable information about the bulk flow of the liquid lead alloy inside the exposure chamber.

II. METHODOLOGY

A. System geometry

The CORELLA facility in its current state enables up to six specimens to be exposed to liquid metal under flowing conditions, with accurate temperature and oxygen control of the liquid metal. The setup of the CORELLA exposure chamber is shown in Fig. 1. It consists of a stationary cylindrical chamber, 300 mm in diameter and 210 mm in height, and a rotating inner cylinder of 160 mm diameter. The height coordinate z is defined to have its origin at the base of the outer cylinder. The base of the inner cylinder is placed at $z = 25$ mm. The inner cylinder rotates with an angular speed Ω of up to 1200 rpm. The chamber is covered by a plate, to which up to six sample holders with specimens can be attached, equally distributed at a radius of 90 mm. The cylindrical sample holders, 10 mm in diameter, range down from the plate to a height of $z = 100$ mm. At the end of each sample holder, a specimen can be fixed. A typical specimen size of $30 \times 9 \times 1.5$ mm^3 is used in this investigation. The specimens are aligned in the flow direction as shown in Fig. 1. The chamber is filled with liquid metal to a height H_0, typically in the range of 150–180 mm, so that the specimens are fully immersed in the liquid metal even under flowing conditions. For this study, a default filling height of 155 mm is used.

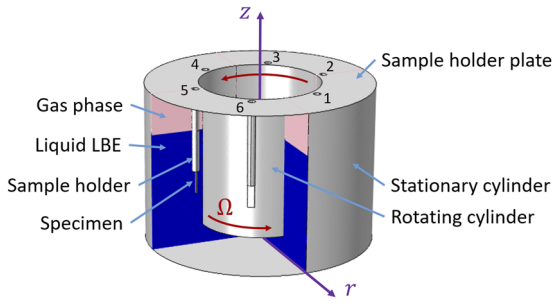

FIG. 1. Setup of the CORELLA exposure chamber with six pairs of sample holders and specimens inserted.

B. Simulation conditions

Numerical simulations of the velocity field inside the CORELLA facility are performed using the software package COMSOL Multiphysics® (COMSOL, Inc., Burlington, MA, USA), a code based on a finite element method. The flow in the gaseous phase above the liquid metal is not taken into account; only single-phase flow of the HLM is considered. Thus, the simulation domain corresponds to the volume filled by the HLM, marked in blue in Fig. 1. However, the free liquid surface, i.e., the interface between the liquid metal and the gaseous phase, is allowed to deform under operation, see Sec. II C. Isothermal incompressible flow is assumed, and a no-slip boundary condition is applied at all solid walls. Full slip is applied at the liquid free surface. Gravity is taken into account. Within the present study, the material properties of liquid LBE are taken at 450 °C.[15] At this temperature, the kinematic viscosity of LBE is of the order of 10^{-7} m^2/s. With a velocity of the order of 1 m/s and the chamber size of the order of 0.1 m, the Reynolds number is of the order of 10^6 and turbulent flow is expected.

For modeling turbulence, the Reynolds averaged Navier–Stokes (RANS) k–ε model is used.[16,17] The standard k–ε model with a high Re number formulation uses wall functions to solve the momentum equations in near-wall regions. This approach requires high Re numbers everywhere to yield accurate results. In addition, it has some limitations in complex geometries where flow separation and recirculation occur. To avoid singularity for (locally) low Re numbers, the wall lift-off in viscous units, δ_w^+, is limited from below by 11.06.[17]

2D rotationally symmetric simulations without any specimens or sample holders inserted are performed in a time-dependent study, i.e., except for the intrinsic time-averaging of small-scale features done in RANS turbulence models, the time evolution of the flow pattern is captured. 3D calculations (with and without specimens) are done for the stationary case only. The rotational speed of the inner cylinder is set to a constant value, and the system is solved for a steady state solution. Potentially evolving large-scale flow patterns are not captured by this approach.

C. Free surface deformation

The free liquid surface experiences deformation due to the combined effects of centrifugal force, gravity, and surface tension. An accurate numerical treatment of the free surface deformation is possible in COMSOL by using either the available free surface feature or the level set method. In the current investigation, the free surface feature combined with a deforming domain and moving mesh is employed in 2D rotationally symmetric simulations, i.e., for the system without any sample holders/specimens inserted. The upper part of the liquid domain is set to a deforming domain with the free liquid surface allowed to move in the vertical direction. Hereby, the pressure balance due to liquid motion, gravity, and surface tension determines the free surface vertical deformation. In order to catch the transient behavior of the flow during start-up, a time-dependent study is performed.

Due to the immense numerical cost of such a computation of the exact free surface deformation in 3D, another route is taken to obtain an approximation of the free surface deformation when sample holders/specimens are introduced. In this approximation, the exact shape of the free surface around the sample holders is

neglected and a rotationally symmetric free surface profile $h(r)$ is assumed. In a first iteration ($n = 0$), the free surface profile $h_1(r)$ is calculated from the azimuthal velocity $v_{\varphi,0}(r)$ of the stationary solution with non-deformed free surface $h_0(r) = H_0$, using the balance of centrifugal force and gravitational force,

$$\frac{dh_{n+1}(r)}{dr} = \alpha_n \frac{v_{\varphi,n}(r)^2/r}{g}.$$

Conservation of mass and a relaxation factor $\alpha_n \leq 1$ for faster convergence of the iteration are taken into account. Using the updated free surface profile h_1, the velocity field $\vec{v}_1$ is computed and the pressure along the free surface h_1 is evaluated. By repeating the described steps, the shape of the rotationally symmetric free surface is adjusted iteratively until the pressure variations along the free surface are minimized. Using this procedure, the approximated free surface $h(r)$, while omitting the small-scale features, still captures accurately enough the change in wetted area and thus the change in drag force compared with the non-deformed free surface. CFD simulations of the 3D system are performed in stationary studies only.

D. Meshing

For the 2D rotationally symmetric study, the simulation domain is divided at a height of $z = 60$ mm in two regions, a lower stationary domain and an upper deforming domain with a moving mesh. The lower domain is meshed using an unstructured triangular mesh with a refinement at the corner of the inner cylinder, while a structured mesh is used in the upper domain. Boundary layers with rectangular cells are added at all walls with no-slip boundary condition. The total number of mesh cells is varied from about 2200 up to about 13 500 domain elements.

The 3D studies do not involve deforming domains and moving meshes; the simulation domain is fixed. Thus, an unstructured tetrahedral mesh is used everywhere in the bulk, with a refinement at the edges and corners of the sample holders, specimens, and rotating cylinder. Boundary layers with prismatic cells are added at all solid walls. The default 3D mesh has about 350 000 domain elements in a 60° wedge with sample holder and specimen. A mesh dependence study is performed including meshes from about 130 000 up to about 750 000 domain elements in the same wedge.

III. RESULTS

A. Unloaded case

To test the applicability and consistency of the numerical method and to get a first insight into the flow pattern and shape of the free liquid surface, CFD simulations were performed without any specimens or sample holders inside the chamber. This allowed the reduction of the 3D system to a 2D rotationally symmetric system and the calculation of the *in situ* free surface deformation in a fully coupled study. In a time-dependent calculation, the rotational velocity of the inner cylinder was ramped up from 0 to the targeted speed Ω over a few seconds and then kept constant for the rest of the simulation until a stationary flow and a stationary shape of the free surface were achieved. The calculations were performed for Ω values of 200, 500, 800, and 1100 rpm.

1. Assessment of numerical method

Before presenting the results, the applicability of the k–ε turbulence model with high Re number formulation (use of wall functions), the mesh resolution in near-wall regions, and the mesh dependence are critically assessed.

The lowest rotational speed studied (Ω = 200 rpm) is the most critical one regarding the Re number. Therefore, the wall lift-off in viscous units δ_w^+ is evaluated for this case. For the mesh with the lowest number of cells tested, the low Re number cutoff of $\delta_w^+ = 11.06$ is active only close to the symmetry axis, for radii below 20 mm. Here, the wall lift-off δ_w reaches 0.45 mm on the axis of both outer and inner cylinders and drops rapidly within the first 10 mm to the value set by the mesh resolution, $\delta_w = y/2$ (here about 0.1 mm for the coarsest mesh). Because the low Re number region is small compared with the entire simulation domain and because the wall lift-off δ_w in this critical region is small compared with the system dimension in this area (25 mm distance between the bases of the two cylinders), the use of the k–ε model with high Re formulation seems appropriate.

The wall lift-off in viscous units should be around 25 for the highest accuracy, while for δ_w^+ values above 100 or several 100, the accuracy might drop significantly.[17] For the coarsest mesh with 2200 domain elements, δ_w^+ varies between about 40 (locally up to 80) for Ω = 200 rpm and about 200 (locally up to 450) for Ω = 1100 rpm. The finest mesh with 13 500 domain elements results in much lower δ_w^+ values, below 60 even for Ω = 1100 rpm. Only very close to the free liquid surface, values up to 160 are obtained at the wall of the outer cylinder. A comparison of the calculation results for the different meshes shows that the flow velocity in near-wall regions strongly depends on the mesh resolution as expected for a treatment with wall functions, see an example for Ω = 500 rpm in Fig. 2. The bulk flow, however, shows a very small mesh sensitivity, with a relative deviation of less than 2% between the coarsest and the finest mesh investigated (3% deviation for 1100 rpm). Hereby, as the mesh resolution increases, the bulk velocity increases and converges toward the solution obtained with the finest mesh.

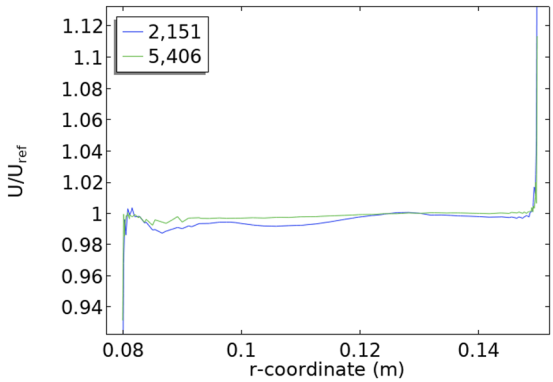

FIG. 2. Mesh dependence study of 2D simulations for 500 rpm. The velocity magnitude U along a horizontal line at z = 0.08 m is shown relative to the results obtained for the finest mesh with 13 549 domain elements, U_{ref}.

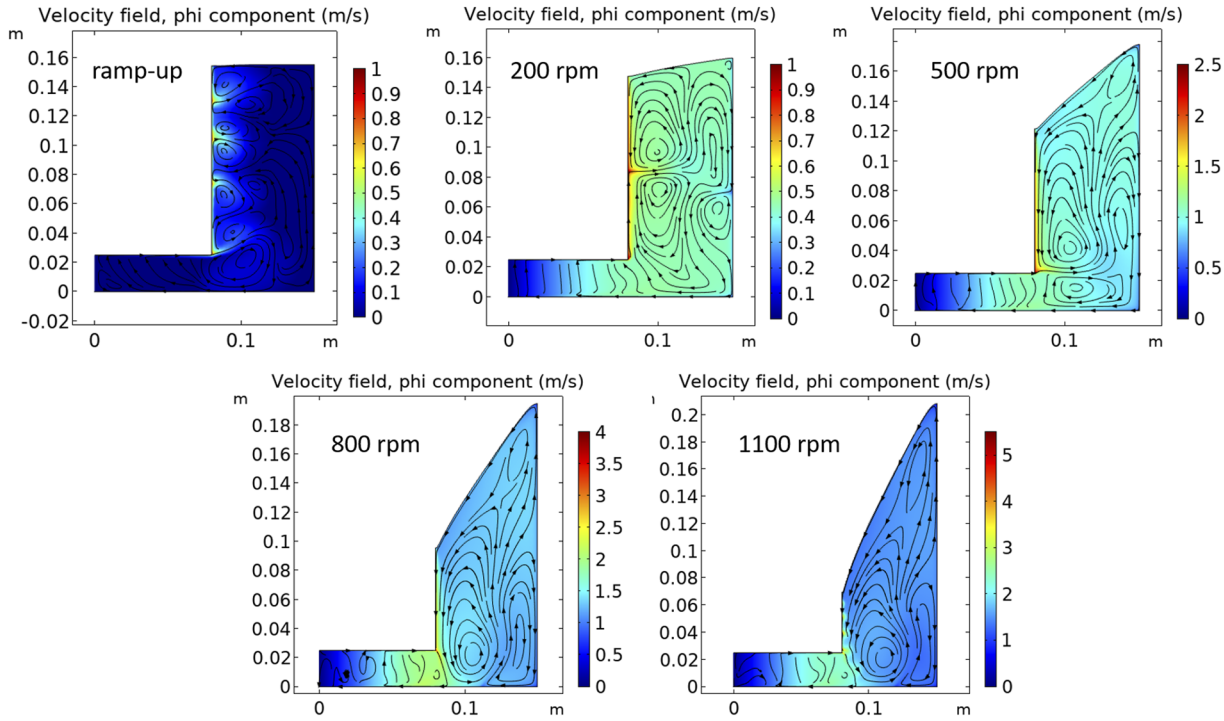

FIG. 3. Flow pattern of 2D rotationally symmetric study during ramp-up and in the stationary stage for rotational speeds as indicated. The color represents the azimuthal velocity component, and the streamlines show the slow rolling motion in non-azimuthal directions.

2. Rotationally symmetric solution

During start-up, both the free surface deformation and the flow pattern evolve until a stable stationary stage is obtained, cf. Fig. 3. Hereby, the flow pattern shows an instability near the inner cylinder. The flow plumes move toward each other and coalesce until the pattern becomes stationary. This flow instability at start-up is known in the literature as the centrifugal instability of the boundary layer at the inner cylinder, see, for instance, Ref. 18.

Compared with the total duration of the exposure experiment (typically several 1000 h), the initial ramp-up phase of a few seconds to minutes can be neglected and the stationary stage is of importance. Figure 3 visualizes the free surface deformation and the flow field in the stationary regime. Note that for $\Omega = 1100$ rpm, a quasi-stationary stage is shown, where the near-wall instability at the inner rotating cylinder still evolves. For all Ω values, the azimuthal velocity represented by the color map is almost constant over the entire volume between the inner and the outer cylinder; exceptions are the near-wall regions. The chosen color range is proportional to the respective Ω, which clearly demonstrates that the azimuthal speed in the bulk grows much less than proportional to Ω. The reason is the smaller wetted area of the rotating cylinder and the larger wetted area of the stationary cylinder as Ω increases. The flow pattern formed by the non-azimuthal rolling motion established in addition to the rotational flow is shown by the streamlines. These vortices are similar to the well known Taylor vortices that appear in Taylor–Couette flows, i.e., in the flow of a viscous fluid confined between two rotating cylinders. The shape and size of the vortices change with the rotational speed of the inner cylinder.

Figure 4 compares the azimuthal and non-azimuthal velocity components along a horizontal line at $z = 0.08$ m for $\Omega = 500$ rpm. The azimuthal speed is much larger than the radial and vertical components; the flow is mainly rotational. As already observed in Fig. 3, the azimuthal speed of the fluid is almost constant over a wide range of radial positions. Exceptions are the boundary layers, i.e.,

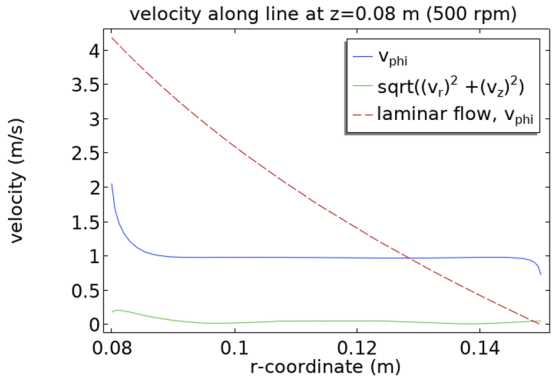

FIG. 4. Profiles of azimuthal and non-azimuthal velocity along the horizontal line at z = 0.08 m for 500 rpm. The dashed line shows the expectation for laminar flow between two rotating cylinders.

the regions close to both cylinder walls. This behavior is typical for turbulent flow in a Taylor–Couette geometry, as elaborated in the following.

Taylor–Couette flows are typically characterized by dimensionless control parameters, such as the Reynolds numbers of the outer and the inner cylinder, the Taylor number, or the ratio of the cylinder radii. With the radius $r_{i,o}$ and the angular velocity $\omega_{i,o}$ of the inner/outer cylinder, the radius ratio is given by $\eta = r_i/r_o$ and the Taylor number is defined as $Ta = (r_o - r_i)^2(r_i + r_o)^2(\omega_i - \omega_o)^2(1+\eta)^4/(64\eta^2\nu^2)$. Here, ν is the kinematic viscosity. For the CORELLA exposure chamber with $r_i = 0.08$ m, $r_o = 0.15$ m, $\omega_i = \Omega$, and $\omega_o = 0$, the radius ratio is $\eta = 0.53$ and $Ta = 2 \times 10^{12}$ for $\Omega = 200$ rpm.

In Taylor–Couette geometry, the flow is laminar for Ta smaller than $\sim 10^4$. The corresponding azimuthal velocity profile $v_\theta \propto (r_o^2 - r^2)/r$ is added as the dashed line to Fig. 4 for comparison. For larger Ta values, turbulent flow is obtained and the flow separates into a bulk flow and two boundary layer flows next to the cylinder walls, the behavior observed in Fig. 4. For $Ta > Ta^*$ ($Ta^* \approx 1 \times 10^{10}$ for $\eta = 0.5$), an ultimate turbulent regime is reached, where the dimensionless angular velocity $\omega' = \omega(r)/\omega_i$ plotted vs the dimensionless radius $r' = (r - r_i)/(r_o - r_i)$ only depends on the radius ratio η. At the midpoint between the outer and the inner cylinder, $r' = 0.5$, the dimensionless angular velocity is 0.20 for $\eta = 0.5$.[19] With $Ta = 2 \times 10^{12}$ for $\Omega = 200$ rpm, the flow in the CORELLA chamber is in the ultimate turbulent regime for all Ω values investigated. The dimensionless angular velocity at the midpoint is 0.19 for $\Omega = 200$ rpm, which is in quite good agreement with the expectation of $\omega' = 0.20$ for Taylor–Couette flows. This further confirms the applicability of the k–ε turbulence model with wall functions for determining the bulk flow in the given system.

3. Consistency checks and 3D solution

The unloaded case represents an ideal system to check the consistency between the two numerical methods proposed for the present study: (i) the fully coupled calculation of the free surface deformation in 2D rotationally symmetric simulations and (ii) the approximation of the free liquid surface by an iterated profile $h(r)$ in three-dimensional studies.

First, in order to test the consistency of the different free surface treatments, the 2D calculations were repeated in a stationary study with the free surface profile $h(r)$ fixed from the previous surface deformation study. The results show an almost constant pressure along the free surface, with some negligible deviations near the cylinder walls due to the neglect of surface tension. The velocity field in the bulk agrees very well with the coupled study performed above, with a deviation of less than 1%.

In a second step, the consistency between 2D and 3D calculations was investigated. The fully three-dimensional flow was solved in a stationary study, where the free surface profile was either fixed from the respective 2D study or adapted to comply with the requirement of a constant pressure. For all Ω tested, a slightly different flow field is obtained when the symmetry constraint is suspended. The flow is not exactly rotationally symmetric. The non-azimuthal rolling motion shows a pattern that deviates from the 2D case as exemplarily shown for 200, 500, and 800 rpm in Fig. 5. Additionally, the azimuthal velocity component and the free surface deformation are generally smaller than in the symmetrically constrained case. The deviation of the velocity in the bulk is below 2% for 200 rpm, while higher deviations are obtained for 500 and 800 rpm (both around 7%). It seems that a rotationally symmetric flow is not the most stable solution, and thus, 3D simulations without symmetry constraint are recommended.

B. Fully loaded case

For all studies containing sample holders and specimens, fully three-dimensional computations were performed and the iterative procedure described in Sec. II C was applied to find a rotationally symmetric approximation of the free liquid surface. In the fully loaded case with six sample holders and specimens inserted, advantage of the system symmetry was taken and a wedge of 60° with periodic boundary conditions was studied. Although the flow in the unloaded case turned out to be not exactly rotationally symmetric, the error introduced by the periodic boundary conditions is expected to be low; see also Sec. III B 3.

1. Assessment of numerical method

As in the 2D rotationally symmetric simulations, the Re number is high enough to justify the use of the k–ε turbulence model with

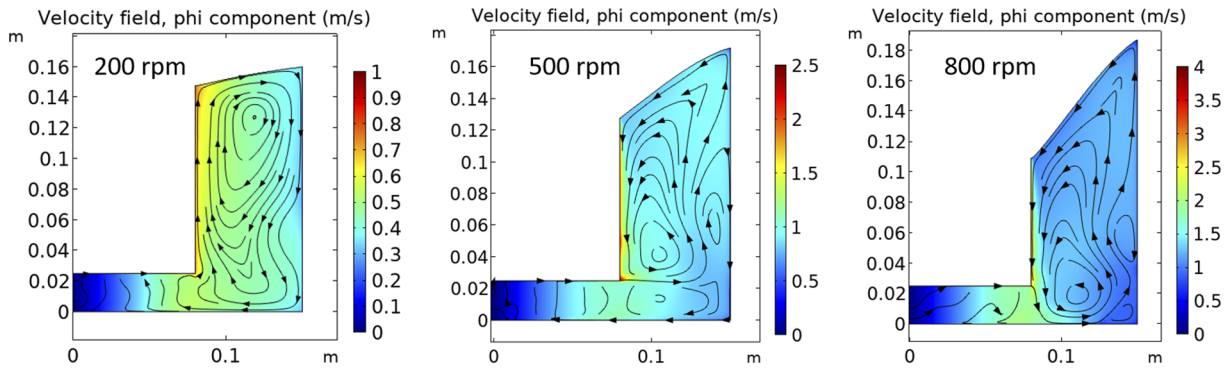

FIG. 5. Stationary flow of the unloaded case obtained in 3D simulations. The color represents the azimuthal velocity component, and the streamlines show the rolling motion in non-azimuthal directions.

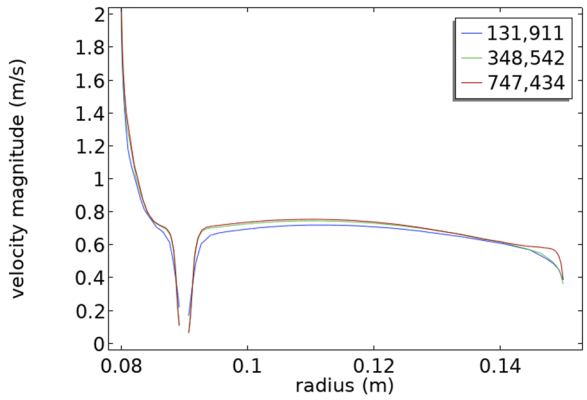

FIG. 6. Results of the mesh dependence study of the fully loaded case for 500 rpm. Velocity magnitude along the horizontal line at z = 0.08 m for different meshes as indicated.

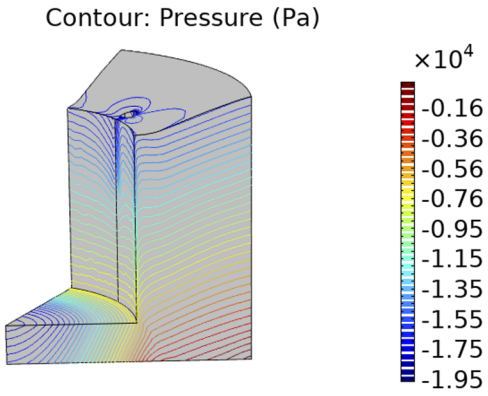

FIG. 7. Pressure distribution for 500 rpm with an approximated rotationally symmetric free surface. The inner cylinder rotates counterclockwise as shown in Fig. 1.

wall functions. Note, however, that flow separation and recirculation might occur around the specimens due to the sudden flow constrictions and expansions. These local flow features are generally not well captured by wall functions.

For the default mesh, the maximum δ_w^+ values are around 160 for the highest speeds investigated (1100 rpm), with correspondingly smaller values for lower speeds and finer meshes. The dependence of the velocity on the mesh refinement is shown exemplarily in Fig. 6 for Ω = 500 rpm along a radial line through the specimen at a height of 0.08 m. Except for the near-wall regions and a larger deviation close to the outer cylinder, the velocity deviation between the default mesh with 348 542 elements and the finest mesh with 747 434 elements is below 2%.

As an example for an iteratively approximated rotationally symmetric free surface, Fig. 7 shows the free surface deformation and the pressure distribution relative to the lower edge of the outer cylinder for 500 rpm. Except for some pressure variations mainly around the sample holder, the pressure is almost constant at the approximated free liquid surface. It therefore can be expected that the approximated free surface reproduces the wetted areas of the inner and the outer cylinder reasonably well.

2. Stationary flow and analysis procedure

Figure 8 presents the results of the flow field for different rotational speeds Ω. In all cases, the specimens are fully wetted by the liquid metal. In addition to the mainly azimuthal flow, a non-azimuthal rolling motion is established, which is visualized by the streamlines in Fig. 8. Similar to the unloaded case presented in Fig. 3, respectively Fig. 5, the velocity magnitude is almost constant in the volume between the inner and the outer cylinder, with the largest decline occurring between the rotating cylinder and the specimens (see also Fig. 6). As expected, the flow is generally slower and thus the free surface deformation is less pronounced than in the unloaded case (Figs. 3 and 5).

Figure 9 shows the velocity magnitude (color map) and streamlines around the specimen on a horizontal plane at z = 0.08 m exemplarily for 500 rpm. Directly at the specimen surface, the fluid velocity decreases to zero due to the no-slip boundary condition. Note that small-scale features of the flow field in near-wall regions, such as flow detachment and recirculation, are not well resolved due to the high Re number k–ε turbulence model used. To get a reasonable value of the tangential speed of the liquid metal bulk flow along

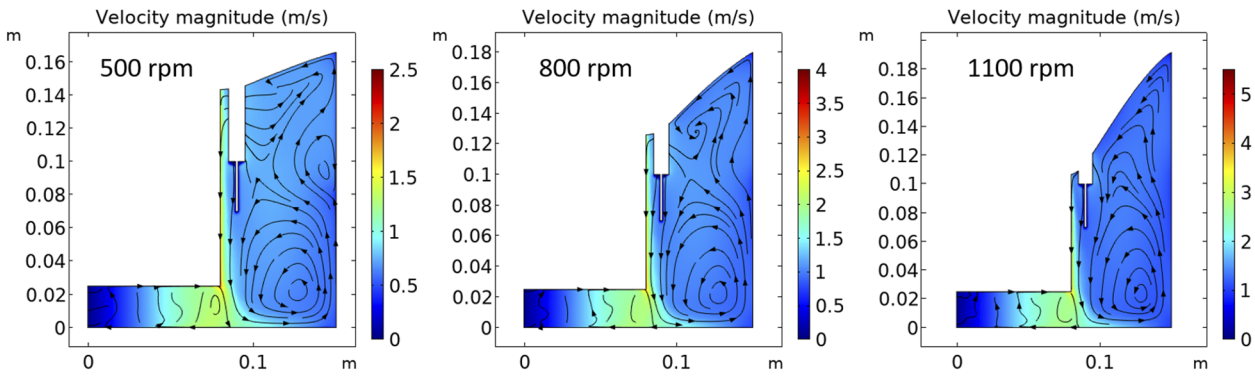

FIG. 8. Flow field of the fully loaded case for 500, 800, and 1100 rpm as indicated. The color represents the velocity magnitude; the streamlines show the non-azimuthal motion.

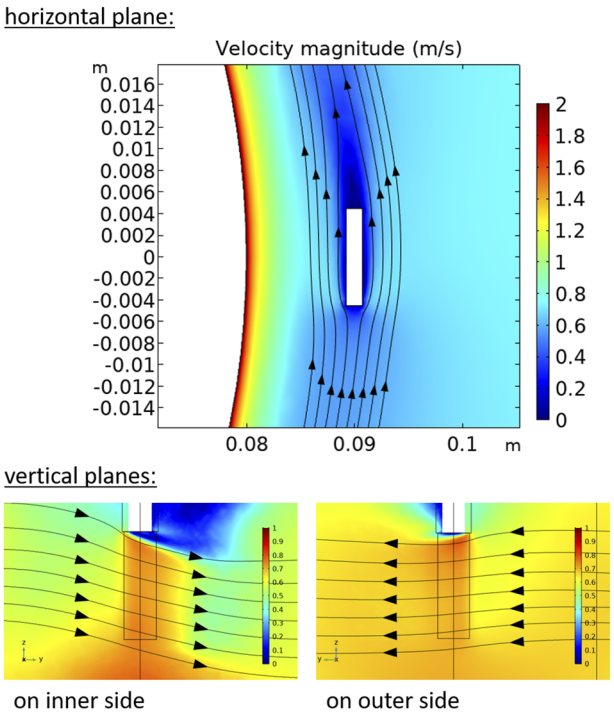

FIG. 9. Visualization of flow around specimens for 500 rpm. Velocity magnitude (color map) and streamlines along the horizontal plane at z = 0.08 m and along vertical planes of interest on inner respectively outer side of specimen as seen from outside respectively inside.

the specimen's lateral surfaces, a distance of 3 mm from the specimen surfaces is chosen for further analysis. Figure 9 visualizes the streamlines on these vertical planes of interest.

On the vertical planes of interest, the average speed next to the lateral surfaces of the specimen was determined. Hereby, the topmost part of the specimen with strongly deviating velocity was excluded. The results are summarized in Fig. 10, together with the values for the fictive case of a horizontally fixed free liquid surface without deformation, $h(r) = H_0$. The influence of the free surface deformation and thus of the change in the wetted area of the rotating inner and stationary outer cylinder on the flow velocity becomes apparent. Also added to Fig. 10 are the data for a filling height of 180 mm instead of the default 155 mm. The higher driving force due to the increased wetted area of the rotating cylinder causes an increased speed on the inner side of the specimens. For radii beyond the sample holders/specimens, however, the larger drag of the sample holders counterbalances the higher driving force. Almost the same velocity as for the default filling height is obtained on the outer side of the specimen.

3. Periodicity assumption

So far, the fully loaded case was solved only in a 60° wedge with periodic boundary conditions. In order to investigate the consistency of this symmetry assumption, the fully loaded case was simulated for a 120° wedge. In addition, a partially loaded case with three pairs of sample holders and specimens symmetrically distributed in

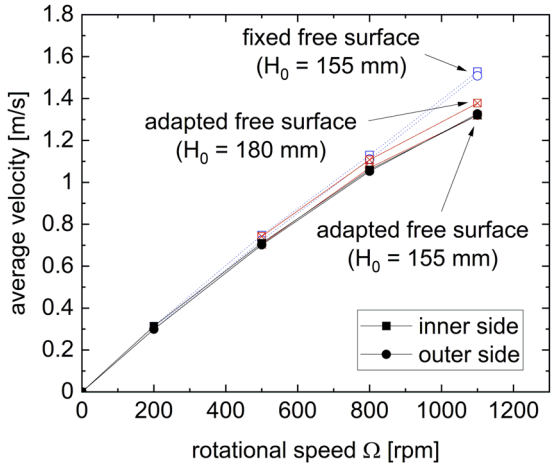

FIG. 10. Results of the fully loaded case. Average speed on inner (squares) and outer (circles) sides of specimen vs rotational speed of the inner cylinder. For the default filling height of 155 mm, filled black symbols show the data for an iteratively adapted rotationally symmetric free surface profile and open blue symbols represent the results for a non-adapted horizontal free surface $h(r) = H_0$. Crossed red symbols show the results for a filling height of 180 mm with adapted free surface.

the chamber was investigated. Here, a 120° wedge and the full 360° system were solved.

Without any symmetry constraint (360° with three specimens) or with a less strict constraint (120° wedge containing two specimens for a total of six specimens), a small variation of the velocity from specimen to specimen is obtained, see Fig. 11. Although this fluctuation is not captured when periodic boundary conditions are applied (120° wedge containing one specimen for a total of three specimens

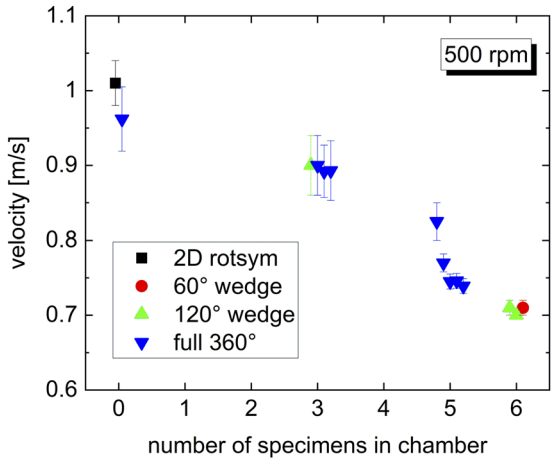

FIG. 11. Comparison of all investigated configurations at 500 rpm. The symbols represent the mean value of the average speeds on the inner and the outer side of the specimens, and the bars mark the difference between the two values. Data from different studies and for different specimens within one study are slightly displaced against each other in the x direction.

or 60° wedge containing one specimen for a total of six), the data are consistent and the use of the periodicity assumption is justified.

C. Comparison of all data at 500 rpm

To summarize and to visualize the influence of the sample loading on the velocity in the CORELLA exposure chamber, all results for a rotational speed of $\Omega = 500$ rpm are compared in Fig. 11. For clarity, the data in Fig. 11 show the mean value of the inner and outer average velocities, with the bars marking the difference between these two values. Note that the same positions were used for evaluation of the average velocities in the unloaded case. As expected, the more sample holders and specimens are inserted in the chamber, the smaller the velocity is. In addition, the velocity difference between inner and outer positions decreases for higher loading.

As an example of a loading without any symmetry, the situation with five pairs of sample holders and specimens was investigated and is added to Fig. 11. The respective data points are slightly displaced in the x direction in the order of the specimen number. The highest velocity is found on the inner side of specimen no. 1, i.e., the specimen against which the liquid metal streams first. The more specimens the fluid passes, the lower its velocity becomes.

Also added to Fig. 11 are the results of the previous consistency checks. As discussed above in Sec. III B 3, the periodicity constraint has only a minor influence on the results. This is demonstrated for the full loading and the partial loading with three specimens. In contrast to the periodicity constraint, the assumption of a rotationally symmetric flow in the unloaded case poses a much stricter constraint and leads to higher deviations, see also Sec. III A 3.

IV. DISCUSSION

The objective of the current research was to obtain reliable information about the bulk flow in the exposure chamber of the CORELLA test stand without and with specimens inserted. To achieve this goal, the present study used the standard k–ε model with high Re number formulation (wall functions). A quantitative comparison of the unloaded case with the flow in the classical Taylor–Couette geometry confirmed the applicability of this approach.

When specimens are inserted, the flow experiences sudden constrictions and expansions around the specimens, which may lead to complex flow phenomena, such as flow separation, reattachment, and recirculation. An accurate study of such phenomena requires a highly resolved mesh in near-wall regions and a turbulence model with low Re number formulation, which solves the velocity profile down to the wall. In some preliminary studies using the low Re number Menter Shear Stress Transport turbulence model or a low Re extension of the k–ε model, it was found that the near-wall flow around the specimens is very sensitive to the exact shape and positioning (azimuthal alignment) of the specimens. The bulk flow, however, remains close to the results presented in this paper.

In addition to a well-resolved velocity field in near-wall regions, turbulence models with low Re formulation also yield more reliable data on the local wall shear stress, near-wall turbulence level, and mass transport of dissolved species across the boundary layers. These parameters can be relevant in erosion and flow-accelerated corrosion in turbulent flows, see, for instance, Ref. 20. Highly resolved numerical studies become relevant also for the CORELLA exposure chamber once a specific experimental situation is analyzed and experimental corrosion data are available for comparison. For the present study, however, the use of the high Re k–ε turbulence model suffices.

An exact treatment of the free liquid surface deformation at an acceptable numerical cost is feasible only for 2D rotationally symmetric simulations. In 2D, however, obstacles, such as sample holders and specimens, cannot be included in the calculation. In addition, considerable deviations were found due to the very strict constraint of a rotationally symmetric flow. To solve the flow in 3D, the free liquid surface was approximated by a rotationally symmetric profile, minimizing the pressure variations along the free surface. Although this procedure cannot predict the free liquid surface around the sample holders very accurately (see Fig. 7), it reproduces reasonably well the wetted areas of the rotating and stationary cylinder walls. As shown in Fig. 10, the liquid velocity indeed changes due to the free surface adaptation.

The flow in the exposure chamber of CORELLA was found to be highly turbulent even for $\Omega = 200$ rpm, the lowest rotational speed of the inner cylinder investigated. Turbulent flow results in a substantially lower velocity at the specimen position than expected for laminar flow, see Fig. 4. This knowledge is relevant for the interpretation of experimental corrosion erosion data. The highest flow velocities along the specimens' lateral surfaces that are experimentally achievable in the CORELLA facility are around 1.3–1.4 m/s (Fig. 10) for the fully loaded case with six sample holders and specimens inserted. If less obstacles hinder the free flow of the liquid metal in the chamber, i.e., in the case of partial loading, the maximum flow speed might be slightly increased, similar to the case of $\Omega = 500$ rpm shown in Fig. 11. However, even in the unloaded case presented in Fig. 3, the speed at the designated specimen position does not exceed 1.5 m/s for $\Omega = 1100$ rpm.

In the present study, the properties of the liquid metal were fixed at typical values (LBE at 450 °C). The use of other liquid metals (e.g., pure Pb) or exposure at other temperatures changes the liquid properties. However, a significant influence on the flow field is expected only for a much higher kinematic viscosity and a much lower Ta number. As long as $Ta > 10^{10}$, the flow is highly turbulent and thus independent of the liquid properties.

Similar to the filling height, also the dimensions of the sample holders and specimens were fixed at typical values, as were their positions and azimuthal alignments. When varying any of these parameters, some changes to the flow are expected. An azimuthal misalignment changes the relation between the speed on the inner side and the speed on the outer side of the respective specimen. Smaller sample holders and specimens or a higher vertical position pose less resistance to the flow and result in slightly higher speeds. Positioning the samples at larger radii or increasing the number of samples to more than six leads to slightly lower speeds along the specimens' lateral sides.

For a more accurate prediction of the bulk flow, the simulations can be easily adapted to the individual experimental conditions of the corrosion erosion experiments of interest. For most experimental studies, however, the results presented in this investigation are accurate enough for an initial interpretation of the experimental findings.

V. SUMMARY AND CONCLUSION

The CORELLA facility enables the investigation of combined corrosion erosion effects in liquid lead alloys with controlled oxygen content and temperature. For an adequate interpretation of the experimental results, however, knowledge of the velocity field inside the exposure chamber is required. The presented CFD study solved the turbulent flow inside the CORELLA exposure chamber for typical liquid metal properties (LBE at 450 °C) and typical specimens' dimensions and positions. Hereby, the free liquid surface was approximated by a rotationally symmetric profile. This approach allowed us to obtain a realistic variation of the wetted areas for different flow conditions and thus to obtain reasonable results for the flow field. The rotational speed of the inner cylinder was varied from 200 up to 1100 rpm, which is close to the experimental limit of stable flow conditions. The chamber loading was varied from the unloaded case up to a loading with six pairs of sample holders and specimens. For all cases studied, the bulk flow was analyzed and the tangential speed along the lateral sides of the specimens was determined. The flow inside the exposure chamber was found to be highly turbulent, with velocities at the specimens' positions much lower than expected for laminar flow. Even for the highest feasible speed of the inner cylinder (1200 rpm), the liquid metal velocity experienced by the specimens does not exceed 1.5 m/s. However, the flow in the CORELLA chamber is not comparable with simple pipe flow at the same bulk speed. Due to the sudden flow constriction and expansion around the specimens, complex flow phenomena, such as flow detachment and recirculation, occur. This leads to a high level of near-wall turbulence and can strongly affect corrosion erosion.

ACKNOWLEDGMENTS

This paper was supported by the European Union's Horizon 2020 research and innovation program under Grant Agreement No. 755269, project GEMMA (GEneration iv Materials MAturity).

DATA AVAILABILITY

The data that support the findings of this study are available from the corresponding author upon reasonable request.

REFERENCES

[1]J. Pacio and T. Wetzel, "Assessment of liquid metal technology status and research paths for their use as efficient heat transfer fluids in solar central receiver systems," Sol. Energy **93**, 11–22 (2013).
[2]A. Heinzel, W. Hering, J. Konys, L. Marocco, K. Litfin, G. Müller, J. Pacio, C. Schroer, R. Stieglitz, L. Stoppel, A. Weisenburger, and T. Wetzel, "Liquid metals as efficient high-temperature heat-transport fluids," Energy Technol. **5**, 1026–1036 (2017).
[3]C. Schroer, O. Wedemeyer, J. Novotny, A. Skrypnik, and J. Konys, "Selective leaching of nickel and chromium from type 316 austenitic steel in oxygen-containing lead–bismuth eutectic (LBE)," Corros. Sci. **84**, 113–124 (2014).
[4]V. Tsisar, C. Schroer, O. Wedemeyer, A. Skrypnik, and J. Konys, "Long-term corrosion of austenitic steels in flowing LBE at 400 °C and 10^{-7} mass% dissolved oxygen in comparison with 450 and 550 °C," J. Nucl. Mater. **468**, 305–312 (2016).
[5]K. Lambrinou, E. Charalampopoulou, T. Van der Donck, R. Delville, and D. Schryvers, "Dissolution corrosion of 316L austenitic stainless steels in contact with static liquid lead-bismuth eutectic (LBE) at 500 °C," J. Nucl. Mater. **490**, 9–27 (2017).
[6]J. Zhang, "A review of steel corrosion by liquid lead and lead–bismuth," Corros. Sci. **51**, 1207–1227 (2009).
[7]F. Martín-Muñoz, "Compatibility of structural materials with lead-bismuth eutectic and lead: Standardisation of data, corrosion mechanism and rate," in *Handbook on Lead-Bismuth Eutectic Alloys and Lead Properties, Materials Compatibility, Thermal-Hydraulics and Technology–2015 Edition* (OECD, 2015), Chap. 6, NEA No. 7268.
[8]L. Martinelli, T. Dufrenoy, K. Jaakou, A. Rusanov, and F. Balbaud-Célérier, "High temperature oxidation of Fe–9Cr–1Mo steel in stagnant liquid lead–bismuth at several temperatures and for different lead contents in the liquid alloy," J. Nucl. Mater. **376**, 282–288 (2008).
[9]A. Weisenburger, C. Schroer, A. Jianu, A. Heinzel, J. Konys, H. Steiner, G. Müller, C. Fazio, A. Gessi, S. Babayan, A. Kobzova, L. Martinelli, K. Ginestar, F. Balbaud-Célerier, F. J. Martín-Muñoz, and L. Soler Crespo, "Long term corrosion on T91 and AISI1 316L steel in flowing lead alloy and corrosion protection barrier development: Experiments and models," J. Nucl. Mater. **415**, 260–269 (2011).
[10]A. Jianu, R. Fetzer, A. Weisenburger, S. Doyle, M. Bruns, A. Heinzel, P. Hosemann, and G. Mueller, "Stability domain of alumina thermally grown on Fe–Cr–Al-based model alloys and modified surface layers exposed to oxygen-containing molten Pb," J. Nucl. Mater. **470**, 68–75 (2016).
[11]H. Shi, A. Jianu, A. Weisenburger, C. Tang, A. Heinzel, R. Fetzer, F. Lang, R. Stieglitz, and G. Müller, "Corrosion resistance and microstructural stability of austenitic Fe–Cr–Al–Ni model alloys exposed to oxygen-containing molten lead," J. Nucl. Mater. **524**, 177–190 (2019).
[12]H. Shi, R. Fetzer, C. Tang, D. V. Szabó, S. Schlabach, A. Heinzel, A. Weisenburger, A. Jianu, and G. Müller, "The influence of Y and Nb addition on the corrosion resistance of Fe–Cr–Al–Ni model alloys exposed to oxygen-containing molten Pb," Corros. Sci. **179**, 109152 (2021).
[13]M. Kieser, H. Muscher, A. Weisenburger, A. Heinzel, and G. Müller, "Liquid metal corrosion/erosion investigations of structure materials in lead cooled systems: Part 1," J. Nucl. Mater. **392**, 405–412 (2009).
[14]T. Lapauw, B. Tunca, J. Joris, A. Jianu, R. Fetzer, A. Weisenburger, J. Vleugels, and K. Lambrinou, "Interaction of $M_{n+1}AX_n$ phases with oxygen-poor, static and fast-flowing liquid lead-bismuth eutectic," J. Nucl. Mater. **520**, 258–272 (2019).
[15]V. Sobolev and A. Gessi, "Thermophysical and electric properties of liquid lead, bismuth and lead-bismuth eutectic," in *Handbook on Lead-Bismuth Eutectic Alloy and Lead Properties, Materials Compatibility, Thermal-Hydraulics and Technologies–2015 Edition* (OECD, 2015), Chap. 2, NEA No. 7268.
[16]D. Wilcox, *Turbulence Modeling for CFD* (DCW Industries, 1998).
[17]See www.comsol.com for CFD Module–User's Guide.
[18]J. B. Flór, L. Hirschberg, B. H. Oostenrijk, and G. J. F. van Heijst, "Onset of centrifugal instability at a rotating cylinder in a stratified fluid," Phys. Fluids **30**, 084103 (2018).
[19]S. Grossmann, D. Lohse, and C. Sun, "High–Reynolds number Taylor-Couette turbulence," Annu. Rev. Fluid Mech. **48**, 53–80 (2016).
[20]T. Wan and S. Saito, "Flow-accelerated corrosion of type 316L stainless steel caused by turbulent lead–bismuth eutectic flow," Metals **8**, 627 (2018).